Effects of Temporal Density Variation and Convergent Geometry on Nonlinear Bubble Evolution in Classical Rayleigh–Taylor Instability

Introduction

Rayleigh–Taylor (RT) instability develops in a large variety of physical systems, including an imploding shell during inertial confinement fusion experiments[1] and a supernovae explosion in astrophysics.[2] RT instability occurs at the interface between two fluids subject to an acceleration field pointing from the heavier to the lighter fluid.[3] Analytical modeling of such an instability, as well as many other physical phenomena, is based mainly on perturbation methods. In such methods, the equations describing both the physical laws and unknown physical quantities are expanded in a series of small parameters. This allows an approximate solution to otherwise mathematically intractable problems to be obtained. When the amplitude of the interface distortion η between fluids is much smaller than the perturbation wavelength λ (linear perturbation analysis), the small parameter of the perturbation method is $k\eta$, where $k = 2\pi/\lambda$ is the wave number. The hydrodynamic equations in this case can be linearized, yielding an exponential in time perturbation growth.[3] When the distortions are amplified by RT instability to amplitudes comparable to the wavelength, the perturbation series based on $k\eta$ expansion becomes divergent and the expansion breaks down. At such amplitudes a different expansion parameter is needed. It was first proposed in Ref. 4 to use a spatial variable along the fluid interface as a small parameter. The perturbation series in this case gives an approximate analytic solution to the nonlinear problem. Such a solution, however, is valid only locally at the tip of the bubble of the lighter fluid raising into the heavier fluid. Layzer's model, despite its simplicity, has been shown to work remarkably well in describing the nonlinear bubble evolution in classical RT instability.[5–9] Recently[9] the model was extended to arbitrary Atwood numbers $A_T = (\rho_h - \rho_l)/(\rho_h + \rho_l)$, where ρ_h and ρ_l are the densities of heavier and lighter fluids, respectively. The convergence effects have been included in Ref. 10 for cylindrical geometry and in Ref. 11 for spherical geometry in the case of self-similar flow. In addition to the Layzer's theory, other models have been successfully used to study the nonlinear RT evolution (see, for example, Refs. 12 and 13). This article presents a general scaling of the bubble evolution with the flow parameters in planar and spherical geometries for arbitrary temporal density variations and shell trajectories.

The following sections (1) discuss the effects of the temporal density variation on the bubble evolution in the planar geometry and (2) describe the model that predicts the nonlinear perturbation evolution in a spherical geometry.

Planar Geometry: Time-Dependent Density

We consider a fluid with time-dependent uniform density $\rho(t)$ supported in a gravitational field $\mathbf{g}(t)$ by a lighter fluid with density $\rho_l \ll \rho$. The effects of the finite density of the lighter fluid will be neglected in the analysis ($A_T = 1$). The gravity is pointing in the negative z direction. The heavier fluid occupies the upper half of the space with $z > 0$. We choose the unperturbed fluid interface to lie in the (x,y) plane. The regions of the distorted interface where the lighter fluid rises into the heavier fluid are referred to as bubbles; regions where the heavier fluid protrudes into the lighter fluid are referred to as spikes. The standard Layzer's approach[4] deals with the flow at the tip of the bubbles where the vortex motion developed at large perturbation amplitudes has a small effect. Next, introducing a velocity potential $\mathbf{v} = \nabla\Phi$, the mass conservation equation is reduced to Poisson's equation:

$$\nabla^2\Phi = \partial_x^2\Phi + \partial_y^2\Phi + \partial_z^2\Phi = -\frac{\dot{\rho}}{\rho}. \qquad (1)$$

The right-hand side of Eq. (1), neglected in the original Layzer's work,[4] is due to the temporal variation in the fluid density. Such a term, however, was retained previously in the analysis of the linear perturbation evolution.[14,15] In the unperturbed case, Eq. (1) yields the velocity field with the uniform spatial gradient $v_z = z\dot{\rho}/\rho$. One must keep in mind that the Layzer's model deals with flow in the proximity of the fluid interface; therefore, the actual flow is not required to have a uniform velocity gradient throughout the whole region. When the fluid interface is distorted, the perturbations start to grow due to RT instability. To find the perturbation evolution, the

fluid equations and hydrodynamic functions are expanded in powers of $\bar{x}$ near the tip of the bubble (we assume that the center of the bubble is localized at $\bar{x}=0$). Here, $\bar{x}=x$ in two-dimensional perturbed flow and $\bar{x}=r=\sqrt{x^2+y^2}$ in three-dimensional flow. The expansion of the position of the distorted interface $\eta(\bar{x},t)$ gives $\eta(\bar{x},t)=\eta_0(t)+\eta_2(t)\bar{x}^2+\cdots$, where $\eta_0>0$ is the bubble amplitude, and η_2 is related to the bubble curvature R as $\eta_2=-1/(2R)$. The solution of Eq. (1) expanded up to $\bar{x}^2$ takes the form

$$\Phi=\frac{a(t)}{k}\left(1-\tilde{c}_g\frac{k^2\bar{x}^2}{4}\right)e^{-k(z-\eta_0)}-\frac{\dot{\rho}}{2\rho}z^2, \tag{2}$$

where k is the perturbation wave number and $\tilde{c}_g=2$ and $\tilde{c}_g=1$ for two- and three-dimensional geometries, respectively. Note that the standard Layzer's model keeps only terms up to $\bar{x}^2$ in the expansion of hydrodynamic functions. It is sufficient, therefore, to retain only the fundamental harmonic in solution (2) to satisfy such accuracy. For higher-accuracy models, the higher harmonics must be included in the velocity potential.[9] The potential Φ is subject to the following jump conditions at the interface $z=\eta(\bar{x},t)$:

$$\partial_t\eta+v_{\bar{x}}\partial_{\bar{x}}\eta=v_z, \tag{3}$$

$$\partial_t\Phi+\frac{v^2}{2}+g\eta=f(t). \tag{4}$$

Equation (3) is due to mass conservation and the incompressibility condition, and Eq. (4) is the Bernoulli's equation. Here, $f(t)$ is an undetermined function of time and $v^2=v_{\bar{x}}^2+v_z^2$ is the total fluid velocity. Substituting Eq. (2) into boundary conditions (3) and (4) and expanding the latter in powers of $\bar{x}$ yields

$$\frac{d}{dt}(\rho\eta_2)=-\frac{d}{dt}(\rho\eta_0)\frac{\tilde{c}_gk}{4}\left(k+4\frac{\tilde{c}_g+1}{\tilde{c}_g}\eta_2\right), \tag{5}$$

$$\frac{d}{dt}\left[\frac{1}{\rho}\frac{d}{dt}(\rho\eta_0)\right]+\frac{\tilde{c}_gk}{2\rho^2}\left[\frac{d}{dt}(\rho\eta_0)\right]^2$$

$$+\frac{4}{k\tilde{c}_g}(g+\ddot{\eta}_0)\eta_2=0. \tag{6}$$

In the limit of a small perturbation amplitude when $k\eta_0\ll1$, the nonlinear terms are negligible (linear regime) and Eqs. (5) and (6) reduce to a well-known limit,[14,15] $\eta_2^{\text{lin}}=-\tilde{c}_gk^2\eta_0^{\text{lin}}/4$ and

$$\frac{d}{dt}\left[\frac{1}{\rho}\frac{d}{dt}\left(\rho\eta_0^{\text{lin}}\right)\right]-\gamma^2\eta_0^{\text{lin}}=0, \tag{7}$$

where $\gamma(t)=\sqrt{kg(t)}$ is the growth rate and the superscript "lin" denotes perturbed quantities in the linear regime. An approximate solution of Eq. (7) can be found in the limit $\dot{\rho}/\rho\ll\gamma$ using the Wentzel–Kramers–Brillouin (WKB) method.[16] According to such a method, the solution is sought in the form $\eta_0^{\text{lin}}=e^{S(t)/\epsilon}$, where

$$\epsilon\sim\max\left[\left(\gamma t_\rho\right)^{-1},\left(\gamma t_\gamma\right)^{-1}\right]\ll1$$

is a small parameter and $t_\rho=\rho/\dot{\rho}$ and $t_\gamma=\gamma/\dot{\gamma}$ are characteristic time scales of the density and growth-rate variation. Then, up to the first order in ϵ, Eq. (7) has the solution

$$\frac{\dot{S}(t)}{\epsilon}=\pm\gamma-\frac{1}{2}\left(\frac{\dot{\rho}}{\rho}+\frac{\dot{\gamma}}{\gamma}\right). \tag{8}$$

Using Eq. (8), the physical optics approximation of η_0 becomes

$$\eta_0^{\text{lin}}=\sqrt{\frac{\rho(0)\gamma(0)}{\rho(t)\gamma(t)}}\left[c_1e^{\int_0^t\gamma(t')dt'}+c_2e^{-\int_0^t\gamma(t')dt'}\right], \tag{9}$$

where integration constants c_1 and c_2 depend on the initial amplitude $\eta_0(0)$ and the initial bubble velocity $\dot{\eta}_0(0)$:

$$c_1=\frac{\eta_0(0)}{2}\left[1+\frac{1}{2\gamma}\left(\frac{\dot{\rho}}{\rho}+\frac{\dot{\gamma}}{\gamma}\right)\right]_{t=0}+\frac{\dot{\eta}_0(0)}{2\gamma(0)},$$

$$c_2=\frac{\eta_0(0)}{2}\left[1-\frac{1}{2\gamma}\left(\frac{\dot{\rho}}{\rho}+\frac{\dot{\gamma}}{\gamma}\right)\right]_{t=0}-\frac{\dot{\eta}_0(0)}{2\gamma(0)}.$$

When the perturbation amplitude becomes large enough, $k\eta_0 > 1$, the bubble growth slows down from the exponential [Eq. (9)] to a power-law dependence. At such amplitudes, the nonlinear terms cannot be neglected (nonlinear regime), and Eqs. (5) and (6) can be solved in the limit $|\dot{\rho}|/\rho \ll \sqrt{kg}$ and $|\dot{\eta}_0/\eta_0| \gg \dot{\rho}/\rho$. The leading-order solution of Eq. (5) becomes $\eta_2^{\mathrm{nl}} = -\tilde{c}_g k/4(1+\tilde{c}_g)$, where the superscript "nl" denotes the perturbations in the nonlinear regime. Substituting η_2^{nl} into Eq. (6) gives

$$-\frac{2}{\tilde{c}_g+1}\dot{a}+ka^2-\frac{2}{\tilde{c}_g(1+\tilde{c}_g)}\left(\frac{\dot{\rho}}{\rho}a+g\right)$$

$$=-\frac{2\rho\eta_0}{\tilde{c}_g(1+\tilde{c}_g)}\frac{d}{dt}\left(\frac{\dot{\rho}}{\rho^2}\right), \tag{10}$$

where $a(t)=-d_t(\rho\eta_0)/\rho$ is the amplitude of the velocity potential defined in Eq. (2). The perturbation growth in the nonlinear regime changes from the exponential to a power law; therefore, $ka^2 \gg \dot{a}$ and the first term in Eq. (10) can be neglected. Then, keeping the terms up to order t_ρ^{-1} in Eq. (10) yields

$$\frac{d\left(\rho\eta_0^{\mathrm{nl}}\right)}{dt}=-\frac{\dot{\rho}}{2kC_g}+\frac{\rho\gamma(t)}{\sqrt{C_g k}}, \tag{11}$$

where $C_g=\tilde{c}_g(1+\tilde{c}_g)/2$. Integrating Eq. (11) leads to

$$\eta_0^{\mathrm{nl}}(t)=\frac{1}{\sqrt{C_g k}\,\rho(t)}\int_{t_s}^{t}\rho(t')\gamma(t')dt'$$

$$+\eta_S\frac{\rho_s}{\rho(t)}+\frac{\rho_s/\rho(t)-1}{2C_g k}, \tag{12}$$

where t_s is the saturation time, $\rho_s = \rho(t_s)$, and $\eta_S = \eta_0(t_s)$ is the bubble amplitude at the saturation time (saturation amplitude). Following Ref. 4, the saturation amplitude can be estimated by equating the bubble velocities $\dot{\eta}_0$ calculated in the linear and nonlinear regimes using Eqs. (9) and (11), respectively. The result takes the form

$$\eta_S=\frac{1}{\sqrt{C_g k}}\left\{1+\frac{1}{2\gamma}\left[\frac{\dot{\gamma}}{\gamma}-\frac{\dot{\rho}}{\rho}\left(1+\frac{1}{\sqrt{C_g}}\right)\right]\right\}_{t=t_s}. \tag{13}$$

Thus, to the lowest order, $\eta_S = 1/\sqrt{C_g k}$ and Eq. (12) becomes

$$\eta_0^{\mathrm{nl}}(t)=\eta_S\frac{\rho_s}{\rho(t)}\left\{\int_{t_s}^{t}\frac{\rho(t')}{\rho_s}\gamma(t')dt'\right.$$

$$\left.+1+\frac{1}{2\sqrt{C_g}}\left[1-\frac{\rho(t)}{\rho_s}\right]\right\}$$

$$=\frac{1}{\rho(t)}\int_{t_s}^{t}\rho(t')U_{\mathrm{L}}(t')dt'$$

$$+\eta_S\left\{\frac{\rho_s}{\rho(t)}+\frac{1}{2\sqrt{C_g}}\left[\frac{\rho_s}{\rho(t)}-1\right]\right\}, \tag{14}$$

where

$$U_{\mathrm{L}}(t)=\sqrt{\frac{g(t)}{C_g k}} \tag{15}$$

is the Layzer velocity. It is convenient in many applications to express the nonlinear bubble evolution in terms of the linear perturbation growth.[17] For the large linear growth factors $[\eta_0 \gg \eta_0(0)]$, Eq. (9) can be rewritten as

$$\eta_0^{\mathrm{lin}}(t)\simeq\eta_S\sqrt{\frac{\rho_s\gamma(t_s)}{\rho(t)\gamma(t)}}e^{\int_{t_s}^{t}\gamma(t')dt'}. \tag{16}$$

Taking the logarithm of both sides in the last equation yields

$$\int_{t_s}^{t}\gamma(t')dt'=\ln\frac{\eta_0^{\mathrm{lin}}(t)}{\eta_S}+\frac{1}{2}\ln\frac{\rho(t)\gamma(t)}{\rho_s\gamma(t_s)}. \tag{17}$$

The second term in the right-hand side of Eq. (17) is logarithmically small at large times with respect to the first term and can be neglected without a significant loss in accuracy. With the help of Eq. (17), the nonlinear bubble amplitude (14) can be rewritten in terms of the linear perturbation growth:

$$\eta_0^{\mathrm{nl}} \simeq \eta_S \left\{ \ln \frac{\eta_0^{\mathrm{lin}}(t)}{\eta_S} - \int_{t_s}^{t} \ln\left[\frac{\eta_0^{\mathrm{lin}}(t')}{\eta_S}\right] \frac{\dot{\rho}(t')}{\rho(t)} dt' \right.$$

$$\left. + \frac{\rho_s}{\rho(t)} + \frac{1}{2\sqrt{C_g}} \left[\frac{\rho_s}{\rho(t)} - 1\right] \right\}. \qquad (18)$$

The saturation time t_s is easily obtained using Eq. (9):[7]

$$\int_0^{t_s} \gamma(t')dt' - \frac{1}{2}\ln\left[\frac{\gamma(t_s)\rho_s}{\rho(0)\gamma(0)}\right] = \ln\left(\eta_S/c_1\right). \qquad (19)$$

The second term in the left-hand side of Eq. (19) has a weak logarithmic time dependence and can therefore be neglected. Substituting $c_1 \simeq \eta_0(0)/2$, Eq. (19) reduces to

$$\int_0^{t_s} \gamma(t')dt' \simeq \ln\frac{2\eta_S}{\eta_0(0)}. \qquad (20)$$

Equation (20) defines the saturation time t_s in terms of the initial amplitude $\eta_0(0)$.

Equation (11) shows that the temporal density variation modifies the asymptotic bubble velocity U_b:

$$U_b \equiv \dot{\eta}_0 \to U_{\mathrm{L}} - \frac{\dot{\rho}}{\rho}\left(\eta_0 + \frac{1}{2C_g k}\right). \qquad (21)$$

In the case of the decompression flow when the density decreases in time $\dot{\rho} < 0$, the bubble grows faster, and, in the case of compression $(\dot{\rho} > 0)$, the bubble grows slower than the classical Layzer velocity $U_{\mathrm{L}} = \sqrt{g/kC_g}$.

Next, to validate the results of the analysis, we compare the bubble evolution in the three-dimensional geometry $(\tilde{c}_g = 1)$ calculated using the system (5)–(6) and the results of asymptotic analysis [Eqs. (9) and (14)]. The gravitational field is assumed in the form $g = g_0 \Big/ \left[1 + \left(t/t_g\right)^{s_g}\right]$. The fluid density changes in time as (a) $\rho(t) = \rho_0\left[1 + C_\rho \left(t/t_0\right)^{s_\rho}\right]$ and (b) $\rho(t) = \rho_0(1 + D_\rho \cos \Omega t)$, where s_g and s_ρ are the power indexes for acceleration and fluid density, respectively, and C_ρ, D_ρ, t_0, and Ω are the normalization constants. Figure 102.48 shows a plot of the bubble amplitude calculated for case (a) with $g_0 = 10\ \lambda/t_0^2$, $t_g = t_0$, $s_g = 1$, $s_\rho = 2$, $C_\rho = 0.25$ (solid line), $C_\rho = 0$ (dashed line), and $C_\rho = -0.15$ (dotted line). The initial conditions are $\eta_0(0) = \lambda/200$ and $\dot{\eta}_0(0) = \lambda/(200\ t_0)$. Thick lines represent the exact solutions of Eqs. (5) and (6); thin lines show the WKB solution for $t < t_s$ and the asymptotic solution (14) after $t = t_s$. Note the larger amplification factor of the bubble amplitude in the decompression flow. Figure 102.49 plots the linear (thin lines) and nonlinear (thick lines) perturbation growth. Observe that the value of η_S calculated using

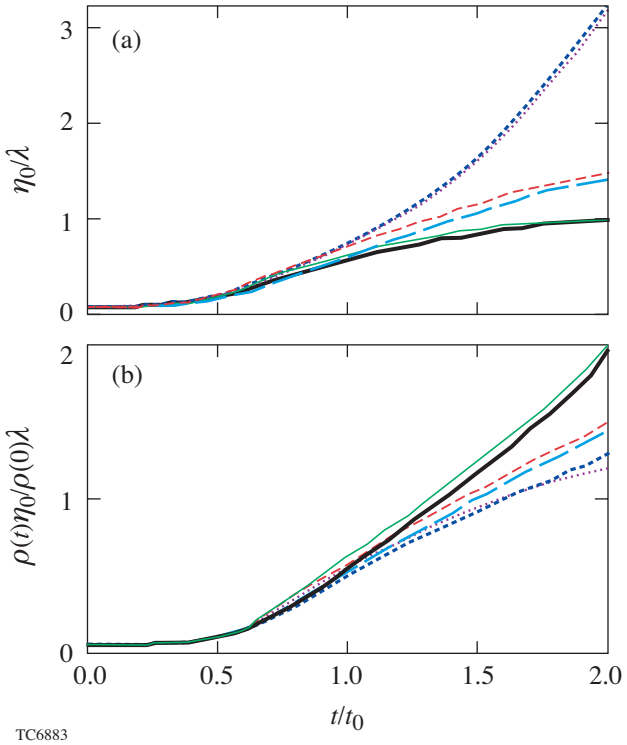

Figure 102.48
Plot of normalized bubble amplitude calculated using the exact numerical solution of Eqs. (5) and (6) (thick lines) and analytical solutions (9) and (14) (thin lines). The solid lines correspond to the fluid compression with $C_\rho = 0.25$, the dashed lines represent the constant density case (classical Layzer's model[4]), and the dotted lines are obtained for the decompression flow with $C_\rho = -0.15$.

Eq. (13) represents a good approximation to the saturation amplitude. The bubble evolution in case (b) is plotted in Fig. 102.50 for D_ρ = 0.3 (solid line) and D_ρ = –0.3 (dashed line). The initial conditions for this case are $\eta_0 = \lambda/2\times10^{-3}$ and $\dot{\eta}_0 = \Omega\lambda/2\times10^{-3}$ and t_g = 1/Ω. A good agreement between the exact solution and the asymptotic formulas validates the accuracy of the performed analysis.

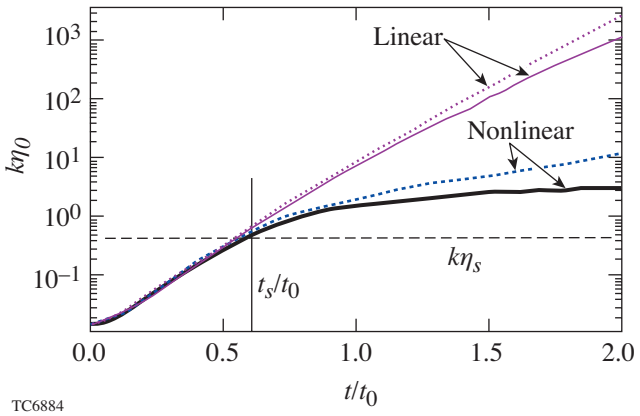

Figure 102.49
Plot of normalized bubble amplitude calculated using the exact numerical solution of Eqs. (5) and (6) with (thick lines) and without (thin lines) nonlinear terms. The solid and dotted lines correspond to C_ρ = 0.25 and –0.15, respectively. The dashed line shows the saturation amplitude defined in Eq. (44).

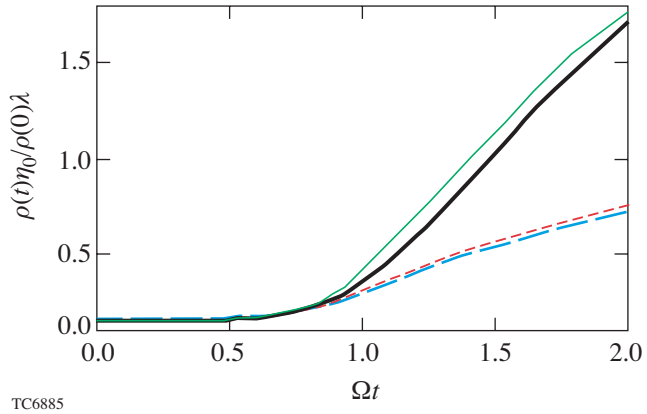

Figure 102.50
Plot of normalized bubble amplitude calculated using the exact numerical solution of Eqs. (5) and (6) (thick lines) and analytical solutions (9) and (14) (thin lines). The solid and dashed lines correspond to D_ρ = 0.3 and –0.3, respectively.

To comment on the effects of temporal density variation on the asymptotic behavior of the Richtmyer–Meshkov (RM) instability, such an instability occurs when a shock passes through a corrugated interface between two fluids. As opposed to RT instability, the instability drive in this case has a finite duration (of the order of the sound-wave propagation across the perturbation wavelength). Thus, the asymptotic evolution of the bubble amplitude can be found using Eq. (10) with g = 0. When the fluid density does not change with time $(\dot{\rho}=0)$, the sum of the first two terms in Eq. (10) must be zero. This yields a decay in time velocity[5,7]

$$\dot{\eta}_0^{\mathrm{RM}} \to U_{\mathrm{L}}^{\mathrm{RM}} = 2\Big/\Big[\big(\tilde{c}_g+1\big)kt\Big]$$

and logarithmically growing bubble amplitude $\eta_0^{\mathrm{RM}} \sim \ln t$. For a finite density derivative, one can attempt to generalize Eq. (14) to RM instability by replacing U_{L} with $U_{\mathrm{L}}^{\mathrm{RM}}$:

$$\eta_0^{\mathrm{RM}} \to \frac{2}{k\big(\tilde{c}_g+1\big)\rho(t)}\int^t \frac{\rho(t')}{t'}dt'. \qquad (22)$$

Equation (22) is the result of balancing the first two terms in Eq. (10) and neglecting its right-hand side. It is easy to show, however, that, opposed to the RT instability, the right-hand side of Eq. (10) cannot be considered small in the RM instability at all times, regardless of the value of $\dot{\rho}/\rho$. Indeed, substituting the constant-density solution into Eq. (10) shows that the first two terms decrease in time (~$1/t^2$), while the right-hand side has a factor of ln t. Thus, even a small density variation can significantly change the asymptotic behavior of the bubble velocity in the RM instability. Although Eq. (22) predicts correctly the trend of the effect, the accuracy of such a scaling is inadequate. To illustrate a strong dependence on the density variation, Fig. 102.51 plots the bubble velocity calculated for densities $\rho = \rho_0$ (dashed line) and $\rho = \rho_0\left[1-\epsilon\left(t/t_0\right)^2\right]$ (solid line), where $\epsilon = 5\times10^{-4}$. The velocities are plotted up to the time when the density difference between two cases is only 10%. The bubble velocity, however, is twice as large with the time-dependent density. The approximate solution (22), shown by the dotted line, gives only half of the decompression effect. For a more accurate estimate, the right-hand side of Eq. (10) must be retained. The solution in this case, however, cannot be written in a closed analytical form for an arbitrary density variation.

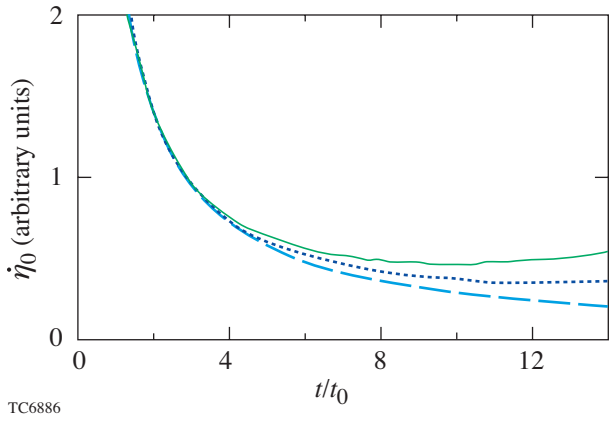

Figure 102.51
The asymptotic bubble velocity for RM instability. The dashed line represents the constant-density solution (~1/t), the solid line is the result of the exact solution of Eqs. (5) and (6) with time-dependent density $\rho=\rho_0\left[1-5\times10^{-4}\left(t/t_0\right)^2\right]$, and the dotted line shows scaling defined in Eq. (22).

Bubble Growth in Spherical Geometry

In a spherical shell of uniform density ρ with an outer radius r_0 and inner radius r_1, the fluid density outside the shell is assumed to be much smaller than ρ (A_T = 1). The shell interfaces are distorted with a single-mode perturbation of the mode number ℓ. To simplify the analysis, a short-wavelength limit was used when the perturbation wavelength was much smaller than the shell thickness $\ell\left(r_0-r_1\right)/r_0\gg1$ or $\ell\gg1$. The perturbations at the inner and outer surfaces in such an approximation are decoupled and can be treated separately. One must keep in mind, however, that even though only a single interface is considered, the product ρr_0^3 is not a constant. If the outer shell boundary is considered, the points where the shell interface has the maximum radii correspond to the perturbation spikes and the points of the minimum radii correspond to the perturbation bubbles. Following Layzer's approach, only the bubble evolution is described. In addition, similar to the analysis in the previous section, the effects due to the surface tension and thermal conduction are neglected.

A bubble is assumed to be symmetric with respect to the polar angle ϕ. The axis of symmetry is along z direction. Solution of the Poisson's equation

$$\nabla^2\Phi=\frac{1}{r^2}\frac{\partial}{\partial r}\left(r^2\frac{\partial\Phi}{\partial r}\right)+\frac{1}{r^2\sin\theta}\frac{\partial}{\partial\theta}\left(\sin\theta\frac{\partial\Phi}{\partial\theta}\right)=-\frac{\dot{\rho}}{\rho} \tag{23}$$

can be written in the form

$$\Phi=\frac{r_0}{\ell}\left[a(t)\left(\frac{r}{r_0}\right)^{\ell}+b(t)\left(\frac{r_0}{r}\right)^{\ell+1}\right]P_{\ell}(\cos\theta)$$

$$-\frac{c(t)}{r}-\frac{\dot{\rho}}{\rho}\frac{r^2}{6}, \tag{24}$$

where P_ℓ is the Legendre polynomial, θ is the azimuthal angle, $a(t)$ and $b(t)$ are undetermined functions of time, and function $c(t)$ is defined by the unperturbed flow condition $\partial_r\Phi\left(r_0\right)=\dot{r}_0$,

$$c(t)=r_0^2\left(\dot{r}_0+\frac{r_0}{3}\frac{\dot{\rho}}{\rho}\right). \tag{25}$$

Here, $\dot{r}_0$ is the velocity of the outer shell boundary. Since terms up to θ^2 are retained in the analysis, only the fundamental harmonic is kept in Eq. (24). In what follows an imploding shell with the unstable outer interface is considered. Thus, $b(t)$ = 0 must satisfy the boundary condition at $\left(r/r_0\right)^{\ell}\to0$. The case of the expanding shell (a = 0) can be treated in a similar fashion and will not be described in detail in this article. Solution (24) must satisfy the boundary condition at $r=r_0+\eta(t,\theta)$, where η is the interface distortion. The first condition is easily derived from the mass conservation equation

$$\dot{\eta}+\frac{v_\theta}{r_0+\eta}\partial_\theta\eta=v_r-\dot{r}_0. \tag{26}$$

Then, assuming a uniform density inside the shell, the momentum equation is integrated to yield Bernoulli's equation

$$-\frac{p}{\rho}=\partial_t\Phi+\frac{1}{2}v^2-f(t), \tag{27}$$

where p is the pressure, $v^2=v_r^2+v_\theta^2$ is the total velocity, and $f(t)$ is an undetermined function of time. Pressure must be continuous across the boundary; therefore, Eq. (27) reduces to

$$\partial_t\Phi+\frac{1}{2}v^2=\tilde{f}(t), \tag{28}$$

where $\tilde{f}(t)=f(t)-p_a(t)/\rho$ and $p_a(t)$ is the drive pressure. To find the distortion amplitude η, the boundary conditions

(26) and (28) and the potential (24) are expanded near the tip of the bubble in series of azimuthal angle θ:

$$\eta(t,\theta)=\eta_0+\eta_2\theta^2+O\left(\theta^4\right),$$

$$P_\ell(\cos\theta)=1-\frac{\ell(\ell+1)}{4}\theta^2+O\left(\theta^4\right). \tag{29}$$

Note that $\eta_0<0$ at the bubble. The resulting system of differential equations takes the form

$$3\frac{d}{dt}\left(\rho r_0^2\eta_2\right)-\frac{2\eta_2}{r_0}\frac{d\left(\rho r_0^3\right)}{dt}\left[1-\left(\frac{r_0}{r_0+\eta_0}\right)^3\right]$$

$$=\left(\frac{r_0}{r_0+\eta_0}\right)^2\frac{d}{dt}\rho\left[\left(r_0+\eta_0\right)^3-r_0^3\right]$$

$$\times\left[\frac{2\ell}{r_0+\eta_0}\eta_2-\frac{\ell(\ell+1)}{4}\right], \tag{30}$$

$$\frac{d}{dt}\left\{\frac{1}{3\rho\left(r_0+\eta_0\right)}\frac{d}{dt}\rho\left[\left(r_0+\eta_0\right)^3-r_0^3\right]\right\}\left(\frac{\eta_2}{r_0+\eta_0}-\frac{\ell+1}{4}\right)$$

$$+\frac{1}{3\rho\left(r_0+\eta_0\right)^2}\frac{d}{dt}\rho\left[\left(r_0+\eta_0\right)^3-r_0^3\right]$$

$$\times\left\{\frac{1}{3\rho\left(r_0+\eta_0\right)^2}\frac{d}{dt}\rho\left[\left(r_0+\eta_0\right)^3-r_0^3\right]\right.$$

$$\times\left[\frac{(\ell+1)^2}{8}-\frac{\eta_2}{r_0+\eta_0}\right]-\left.\frac{\eta_2}{\rho\left(r_0+\eta_0\right)^3}\frac{d}{dt}\left(\rho r_0^3\right)\right\}$$

$$+\frac{\eta_2}{\left(r_0+\eta_0\right)^2}\left\{r_0^2\ddot{r}_0+\left[\left(r_0+\eta_0\right)^3-r_0^3\right]\right.$$

$$\times\left.\left[\frac{2r_0^3}{9\left(r_0+\eta_0\right)^3}\left(\frac{d_t\rho r_0^3}{\rho r_0^3}\right)^2+\frac{4}{9}\left(\frac{\dot{\rho}}{\rho}\right)^2-\frac{\ddot{\rho}}{3\rho}\right]\right\}=0. \tag{31}$$

Although the system (30)–(31) can be easily integrated numerically for a given trajectory $r_0(t)$ and shell density $\rho(t)$, it is difficult to get a physical insight on the convergence effects from this rather cumbersome system. To obtain a scaling of the asymptotic nonlinear bubble amplitude with the flow parameters, the equations can be significantly simplified by assuming that the bubble amplitude is much smaller than the shell radius $|\eta_0|\ll r_0$ (a combination $\ell|\eta_0|/r_0$, however, can be arbitrarily large since $\ell >> 1$). Simple calculations reduce Eqs. (30) and (31) in this case to

$$\frac{d}{dt}\left(\rho r_0^2\eta_2\right)=-\frac{\ell(\ell+1)}{4}\frac{d}{dt}\left(\rho r_0^2\eta_0\right)\left(1-\frac{8}{\ell+1}\frac{\eta_2}{r_0}\right), \tag{32}$$

$$\frac{d}{dt}\left[\frac{d_t\left(\rho r_0^2\eta_0\right)}{\rho r_0}\right]-\frac{\ell+1}{2}\left[\frac{d_t\left(\rho r_0^2\eta_0\right)}{\rho r_0^2}\right]^2-\frac{4\eta_2}{\ell+1}\left(\ddot{r}_0+\ddot{\eta}_0\right)$$

$$=-(\ell+1)\frac{\eta_0^2}{r_0^2}\frac{d_t\left(\rho r_0^2\eta_0\right)}{\rho r_0}\frac{d_t\left(\rho r_0^3\right)}{\rho r_0^3}. \tag{33}$$

The term in the right-hand side of Eq. (33) is retained for the high-convergence-ratio implosions.

When $\ell|\eta_0|/r_0\ll 1$, the nonlinear terms can be neglected, leading to $\eta_2^{\text{lin}}=-\eta_0^{\text{lin}}\ell(\ell+1)/4$. Equation (33) recovers, in this limit, the results of Refs. 15, 18, and 19,

$$\frac{d}{dt}\left(\frac{r_0^2\dot{\xi}_0^{\text{lin}}}{m}\right)+\ell\frac{\ddot{r}_0 r_0}{m}\xi_0^{\text{lin}}=0, \tag{34}$$

where $\xi_0=\rho(t)r_0^2(t)\eta_0$, $m(t)=\rho(t)r_0^3(t)$, and the dot denotes the time derivative. The new function ξ_0 can be related to a very important parameter characterizing the shell stability. In comparing performances of different implosions with respect to the shell breakup, it is not the bubble amplitude itself, but the ratio of the amplitude η_0 to the in-flight shell thickness Δ that must be considered. The parameter $\Upsilon=|\eta_0|/\Delta$ is referred to as an instability factor. Multiplying the denominator and numerator in Υ by ρr_0^2, we obtain $\Upsilon=4\pi|\xi_0|/M_{\text{sh}}$, where $M_{\text{sh}}=4\pi\rho r_0^2\Delta$ is the shell mass. Thus, divided by the shell mass, $|\xi_0|$ shows how close the imploding shell is to

breaking up. If $|\xi_0|/M_{sh} \simeq (4\pi)^{-1}$, the shell integrity is compromised by the instability growth.

An approximate solution of Eq. (34) can be found in the limit $\ell >> 1$ using the WKB method. Writing the solution as $\xi_0^{lin} = e^{S/\epsilon}$ ($\epsilon << 1$ is a small parameter), Eq. (34) becomes

$$\dot{S}^2 + \epsilon\left[\ddot{S} + \left(2\frac{\dot{r}_0}{r_0} - \frac{\dot{m}}{m}\right)\dot{S}\right] + \epsilon^2 \ell \frac{\ddot{r}_0}{r_0} = 0. \tag{35}$$

To satisfy Eq. (35) we must require $\epsilon = 1/\sqrt{\ell}$. Then, expanding S in powers of ϵ, the solution up to the first order in ϵ takes the form

$$S = \pm\int^t \sqrt{-\frac{\ddot{r}_0(t')}{r_0(t')}}\,dt' + \frac{\epsilon}{2}\ln\left(\frac{m}{r_0^2}\sqrt{-\frac{r_0}{\ddot{r}_0}}\right). \tag{36}$$

The WKB solution (36) is valid if the shell acceleration $\ddot{r}_0$ does not go to zero during the implosion. With the help of Eq. (36), ξ_0^{lin} becomes

$$\xi_0^{lin} = \frac{\sqrt{m(t)m(0)}}{r_0(t)}\sqrt{\frac{\Gamma(0)}{\Gamma(t)}} \times\left[C_1 e^{\int_0^t \Gamma(t')dt'} + C_2 e^{-\int_0^t \Gamma(t')dt'}\right], \tag{37}$$

where

$$\Gamma(t) = \sqrt{-\ell\frac{\ddot{r}_0(t)}{r_0(t)}},$$

and the integration constants C_1 and C_2 depend on the initial bubble amplitude $\eta_0(0)$ and bubble velocity $\dot{\eta}_0(0)$,

$$C_1 = \frac{\eta_0(0)}{2}\left\{1 + \frac{1}{2\Gamma(0)}\left[\frac{\dot{m}(0)}{m(0)} + \frac{\dot{\Gamma}(0)}{\Gamma(0)}\right]\right\} + \frac{\dot{\eta}_0(0)}{2\Gamma(0)},$$

$$C_2 = \frac{\eta_0(0)}{2}\left\{1 - \frac{1}{2\Gamma(0)}\left[\frac{\dot{m}(0)}{m(0)} + \frac{\dot{\Gamma}(0)}{\Gamma(0)}\right]\right\} - \frac{\dot{\eta}_0(0)}{2\Gamma(0)}.$$

In the limit of $\ell >> 1$, coefficients C_1 and C_2 in the leading order reduce to $C_1 = C_2 \simeq \eta_0(0)/2$. The perturbations grow according to Eq. (37) until the nonlinear effects become important and the bubble growth slows down (nonlinear saturation). To find the perturbation amplitude η_S at which the transition from linear to nonlinear growth occurs, we must first determine the bubble evolution in the nonlinear regime. Then, equating the linear and nonlinear bubble velocities will define an approximate saturation amplitude.[4]

We begin the nonlinear analysis with Eq. (32), which can be rewritten in the limit $\ell >> 1$ as

$$\dot{\xi}_0\left(1 - 8\epsilon^2\frac{\eta_2}{r_0}\right) = -4\epsilon^4\frac{d}{dt}\left(\rho r_0^2 \eta_2\right), \tag{38}$$

where $\epsilon = 1/\sqrt{\ell}$. The left-hand side of Eq. (38) is of the order of $\epsilon^0\xi_0$; the right-hand side is of the order of $\epsilon^4\eta_2$. It can be shown that to satisfy Eq. (38), we must order $\eta_2^{nl}/r_0 \sim \epsilon^{-2}$. Here, the superscript "nl" denotes the functions in the nonlinear regime. To the lowest order in ϵ, the latter ordering gives $\eta_2^{nl}/r_0 = \ell/8$. Keeping the higher-order terms in η_2^{nl} yields

$$\frac{\eta_2^{nl}}{r_0} = \frac{\ell}{8} + \frac{\dot{m}(t)}{16\,\dot{\xi}_0^{nl}}. \tag{39}$$

For a decreasing $m(t)$ (which is almost always the case in a converging shell), η_2 reaches an asymptotic value that is slightly larger than $r_0\ell/8$ (keep in mind that the bubble amplitude η_0 is negative). The difference between η_2/r_0 and $\ell/8$ decays in time in the case of growing $|\xi_0|$. When the ratio η_0/r_0 cannot be neglected compared to unity, the solution (39), according to Eq. (30), is multiplied by a factor $\left(1 + \eta_0^{nl}/r_0\right)$:

$$\frac{\eta_2^{nl}}{r_0} = \left[\frac{\ell}{8} + \frac{\dot{m}(t)}{16\,\dot{\xi}_0^{nl}}\right]\left(1 - \frac{|\eta_0^{nl}|}{r_0}\right). \tag{40}$$

Such a factor further reduces the asymptotic value of η_2^{nl} at the large bubble amplitudes. A detailed comparison with the

exact numerical solution of Eqs. (30) and (31) shows that η_2^{nl} can be replaced by $r_0\ell/8$ in Eq. (33) without significant loss in accuracy. This yields

$$\ell\left(\dot{\xi}_0^{\mathrm{nl}}\right)^2-\dot{\xi}_0^{\mathrm{nl}}\dot{m}\left[1+2\ell\left(\frac{\xi_0^{\mathrm{nl}}}{m}\right)^2\right]+2\dot{m}\xi_0^{\mathrm{nl}}\frac{\dot{r}_0}{r_0}+\frac{\ddot{r}_0}{r_0}m^2$$

$$=\frac{m^2}{r_0^2}\frac{d}{dt}\left(\frac{\dot{\xi}_0^{\mathrm{nl}}}{\rho r_0}\right)+\xi_0^{\mathrm{nl}}\frac{m^2}{r_0}\frac{d}{dt}\left(\frac{\dot{\rho}}{\rho^2 r_0^2}\right). \tag{41}$$

As in the planar geometry case, $\dot{a}(t)$ can be neglected with respect to $\ell a^2(t)$ in the nonlinear regime, where $a=\dot{\xi}_0/\rho r_0^2$ is the amplitude in the velocity potential defined in Eq. (24). Furthermore, we also drop the second term in the right-hand side of Eq. (41). This term is identically zero at a constant density; if $\dot{m}=0$ (solid sphere implosion), the term is equal to $-3m^2\left(\ddot{r}_0/r_0\right)\left(\eta_0^{\mathrm{nl}}/r_0\right)$, which is smaller by a factor η_0^{nl}/r_0 compared to the last term in the left-hand side of Eq. (41). Next, solving the second-order algebraic equation for $\dot{\xi}_0^{\mathrm{nl}}$ yields

$$\dot{\xi}_0^{\mathrm{nl}}=\dot{m}\left[\frac{1}{2\ell}+\left(\frac{\xi_0^{\mathrm{nl}}}{m}\right)^2\right]$$

$$-\sqrt{\dot{m}^2\left[\frac{1}{2\ell}+\left(\frac{\xi_0^{\mathrm{nl}}}{m}\right)^2\right]^2-\frac{2\dot{m}}{\ell}\frac{\dot{r}_0}{r_0}\xi_0^{\mathrm{nl}}-\frac{\ddot{r}_0}{r_0}\frac{m^2}{\ell}}. \tag{42}$$

As mentioned earlier, the approximate value of the saturation amplitude η_S can be obtained by equating $\dot{\xi}_0$ in the linear and nonlinear regimes. In the linear case, using the WKB solution (37), we write $\dot{\xi}_0=\sqrt{\ell}\dot{S}(t)\xi_0$. This gives

$$\dot{\xi}_0=\xi_0\left[\Gamma(t)+\frac{1}{2}\left(\frac{\dot{m}}{m}-2\frac{\dot{r}_0}{r_0}-\frac{\dot{\Gamma}}{\Gamma}\right)\right]. \tag{43}$$

Substituting Eq. (43) into Eq. (42) and neglecting terms with ξ_0^2 (shell convergence ratio is assumed to be not very large at the time of the bubble saturation, so the terms with ξ_0^2 are small) yields the saturation amplitude

$$\frac{|\eta_S|}{r_0(t_s)}=\frac{|\xi_S|}{m_s}=\frac{1}{\ell}\left[1+\frac{1}{\Gamma}\left(\frac{\dot{\Gamma}}{2\Gamma}+\frac{\dot{r}_0}{r_0}-\frac{\dot{m}}{m}\right)\right]_{t=t_s}, \tag{44}$$

where t_s is the saturation time, $m_s=m(t_s)$, $\eta_S=\eta_0(t_s)$, and $\xi_S=\xi_0(t_s)$. Since $\Gamma\sim\sqrt{\ell}$, the bubble saturation amplitude, to the lowest order in ℓ^{-1}, is $|\eta_S|\sim r_0(t_s)/\ell$. To find the bubble evolution after the saturation, we solve Eq. (42) in the limit of $\ell>>1$, expanding the solution $\xi_0^{\mathrm{nl}}=\xi_{00}+\xi_{01}+\ldots$, where $\xi_{00}/\xi_{01}\sim\sqrt{\ell}\gg 1$. Keeping the lowest-order terms in Eq. (42) gives

$$\xi_{00}=-\frac{1}{\ell}\int_{t_s}^{t}\Gamma(t')m(t')dt'+c_0, \tag{45}$$

where c_0 is an integration constant. Substituting ξ_{00} back into Eq. (42) and retaining the terms of the order $1/\ell$ yields ξ_{01}. Combining ξ_{00} and ξ_{01} and using the saturation condition $\xi_0(t_s)=-m_s/\ell$ leads to

$$\xi_0^{\mathrm{nl}}=-m(t)I(t)+\frac{m(t)-3m_s}{2\ell}$$

$$+\int_{t_s}^{t}\dot{m}\left[I(t')^2-I(t')\frac{\dot{r}_0}{r_0\Gamma}\right]dt', \tag{46}$$

where

$$I(t)=\frac{1}{\ell m(t)}\int_{t_s}^{t}\Gamma(t')m(t')dt'$$

$$=\frac{1}{m(t)}\int_{t_s}^{t}U_{\mathrm{L}}^{\mathrm{sp}}(t')\frac{m(t')}{r_0(t')}dt'$$

and

$$U_{\mathrm{L}}^{\mathrm{sp}}=\sqrt{-\frac{\ddot{r}_0(t)r_0(t)}{\ell}}.$$

Equation (46) can be further simplified by taking the integral by parts,

$$\int_{t_s}^{t} \dot{m}\left[I(t')^2 - I(t')\frac{\dot{r}_0}{r_0\Gamma}\right]dt'$$

$$= m(t)\ln\left[\frac{m(t)}{m_s}\right]\left(I^2 - I\frac{\dot{r}_0}{\Gamma r_0}\right)$$

$$-\int_{t_s}^{t} \ln\frac{m(t')}{m_s}\frac{d}{dt'}\left[m(t')\left(I^2 - I\frac{\dot{r}_0}{\Gamma r_0}\right)\right]dt', \qquad (47)$$

and neglecting the second integral in the right-hand side of Eq. (47). This gives a relatively simple scaling with ~20% error. Substituting Eq. (47) into Eq. (46) and replacing

$$1+\left(\frac{\dot{r}_0}{r_0\Gamma} - I\right)\ln\frac{m(t)}{m_s} \simeq \left[\frac{m(t)}{m_s}\right]^{\dot{r}_0/r_0\Gamma - I}$$

yields

$$\xi_0^{\mathrm{nl}} \simeq -m(t)I(t)\left[\frac{m(t)}{m_s}\right]^{\dot{r}_0/(r_0\Gamma)-I} + \frac{m(t)-3m_s}{2\ell}$$

$$\simeq \xi_s\left\{\left[\frac{m(t)}{m_s}\right]^{\dot{r}_0/(r_0\Gamma)-I}\int_{t_s}^{t}\Gamma(t')\frac{m(t')}{m_s}dt'\right.$$

$$\left. + \frac{3-m(t)/m_s}{2}\right\}$$

$$= -\left[\frac{m(t)}{m_s}\right]^{\dot{r}_0/(r_0\Gamma)-I}\int_{t_s}^{t} U_{\mathrm{L}}^{\mathrm{sp}}(t')\rho(t')r_0^2(t')dt'$$

$$+\xi_S\frac{3-m(t)/m_s}{2}. \qquad (48)$$

To use Eq. (48), one must specify the saturation time t_s. The latter can be easily obtained with the help of Eq. (37). At the time of bubble saturation, the following equality must be satisfied:

$$\frac{m_s}{\ell} \simeq |C_1|\frac{\sqrt{m_s m(0)}}{r_0(t_s)}\sqrt{\frac{\Gamma(0)}{\Gamma(t_s)}}e^{\int_0^{t_s}\Gamma(t')dt'}, \qquad (49)$$

which leads to

$$\int_0^{t_s}\Gamma(t')dt' \simeq \ln\left[\frac{r_0(t_s)}{\ell|C_1|}\sqrt{\frac{m_s\Gamma(t_s)}{m(0)\Gamma(0)}}\right]. \qquad (50)$$

It is sufficient in many cases to keep only the lowest-order terms in Eq. (50). This gives

$$\int_0^{t_s}\Gamma(t')dt' \simeq \ln\left[\frac{r_0(0)}{\ell|C_1|}\right] \simeq \ln\left[\frac{2r_0(0)}{\ell|\eta_0(0)|}\right]. \qquad (51)$$

To obtain a more accurate value of t_s, one must solve Eq. (50).

It is interesting to note that the perturbation growth factors are smaller in a "compact" shell with a larger density than in a decompressed, lower-density shell [$\eta_0 \sim 1/\sqrt{m}$ before and $\eta_0 \sim m^{-I-|\dot{r}_0|/(\Gamma r_0)}$ after the saturation]. The shell thickness Δ, however, is inversely proportional to m; therefore, the ratio $\Upsilon = |\eta_0|/\Delta$ is larger in the higher-density shell [$\Upsilon \sim \xi_0 \sim \sqrt{m(t)}$ in the linear regime and $\Upsilon \sim m(t)$ in the nonlinear regime]. Thus, for the same shell trajectory, the thinner shell is more unstable.

As a next step, the nonlinear bubble evolution is expressed in terms of the linear perturbation growth. The linear growth can be calculated, for example, using the stability postprocessor described in Ref. 15. When the perturbation amplitude is much larger than the initial amplitude $\eta_0(0)$, Eq. (37) can be rewritten as

$$\eta_0^{\mathrm{lin}} \simeq \eta_S\sqrt{\frac{m_s\Gamma(t_s)}{m(t)\Gamma(t)}}e^{\Psi(t)}, \quad \Psi(t) = \int_{t_s}^{t}\Gamma(t')dt', \qquad (52)$$

where $\eta_S \simeq -r_0(t_s)/\ell$ is the saturation amplitude. Then,

$$\Psi(t) = \ln\frac{\eta_0^{\rm lin}}{\eta_S} + \frac{1}{2}\ln\left[\frac{\Gamma(t)m(t)}{\Gamma(t_s)m_s}\right]. \tag{53}$$

The linear RT growth is exponential; thus, assuming that $\Gamma(t)$ and $m(t)$ grow slower than $\eta_0^{\rm lin}$, the second logarithm in the right-hand side of Eq. (53) can be neglected. Function $I(t)$ in Eq. (48) can be rewritten in terms of the function $\Psi(t)$:

$$\ell I(t) = \Psi(t) - \frac{1}{m(t)}\int_{t_s}^{t}\Psi(t')\dot{m}(t')dt'.$$

With the help of the latter relation and substituting $\ell \simeq -r_0(t_s)/\eta_S$, Eq. (48) becomes

$$\eta_0^{\rm nl}(t) = \eta_S\frac{r_0(t)}{r_0(t_s)}\left\{\left[\ln\frac{\eta_0^{\rm lin}(t)}{\eta_S} - \frac{1}{m(t)}\int_{t_s}^{t}\ln\frac{\eta_0^{\rm lin}(t')}{\eta_S}\dot{m}(t')dt'\right]\left[\frac{m_s}{m(t)}\right]^{\alpha_m(t)} + \frac{3}{2}\frac{m_s}{m(t)} - \frac{1}{2}\right\}, \tag{54}$$

where

$$\alpha_m(t) = -\frac{\dot{r}_0\eta_0^{\rm lin}(t)}{r_0\dot{\eta}_0^{\rm lin}} + \frac{|\eta_S|}{r_0(t_s)}\left[\ln\frac{\eta_0^{\rm lin}(t)}{\eta_S} - \frac{1}{m(t)}\int_{t_s}^{t}\ln\frac{\eta_0^{\rm lin}(t')}{\eta_S}\dot{m}(t')dt'\right].$$

Equation (54) is especially simple in the case of a solid-sphere implosion when $m = \rho r_0^3 = \text{const}$,

$$\eta_0^{\rm nl}(t)\Big|_{\rho r_0^3=\text{const}} = \eta_S\frac{r_0(t)}{r_0(t_s)}\left[\ln\frac{\eta_0^{\rm lin}(t)}{\eta_S} + 1\right]. \tag{55}$$

Except for the factor $r_0(t)/r_0(t_s)$, Eq. (55) reproduces the asymptotic formula proposed in Ref. 17.

To validate the accuracy of the derived results, we compare the bubble evolution calculated using the exact system [Eqs. (30) and (31)] with the analytical scaling [Eqs. (37) and (48)]. Figure 102.52(a) plots the bubble amplitude for mode numbers ℓ = 100 and ℓ = 200. The outer shell radius changes according to a power law $r_0 = R_0(1 - t/t_0)^{1/3}$, where $0 \le t < t_0$. The density is inversely proportional to the trajectory,

$$\rho(t) = \rho_0\left[R_0/r_0(t)\right].$$

The initial conditions are

$$\eta_0 = -2\times10^{-4}\,R_0/\ell$$

and

$$\dot{\eta}_0 = 2\times10^{-4}\,R_0/\ell t_0\,.$$

The solid lines represent the exact solution of Eqs. (30) and (31), and dashed lines are obtained using Eq. (37) for $t < t_s$ and Eq. (48) for $t > t_s$. The saturation time t_s is defined as the time of intersection of the linear amplitude [Eq. (37)] with the saturation amplitude [Eq. (44)]. Figure 102.52(b) plots the normalized amplitudes with (solid curves) and without (dashed curves) the nonlinear effects. Observe that the saturation value defined by Eq. (44) reproduces very well the bubble amplitude at which the growth slows down and becomes nonlinear. Figure 102.53 plots the bubble evolution for the shell with $r_0 = R_0\cos\Omega t\,(0 \le \Omega t < \pi/2)$ and mode number ℓ = 200. The initial conditions for the perturbations are the same as in the previous case ($\Omega = 1/t_0$). The density is assumed to follow a power law of the radius, $\rho(t) = \rho(0)\left[R_0/r_0(t)\right]^{s_\rho}$. The thick lines represent the exact numerical solution of Eqs. (30) and (31), and the thin lines are the results of the asymptotic analysis. The solid, dashed, and dotted lines in Fig. 102.53

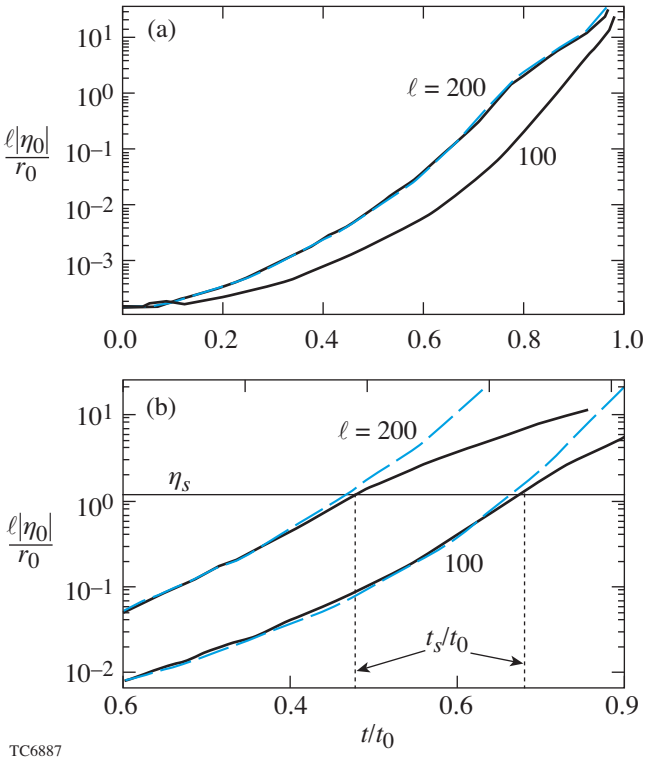

Figure 102.52
(a) Plot of normalized bubble amplitude calculated using the exact numerical solution of Eqs. (30) and (31) (solid lines) and analytical solutions (37) and (48) (dashed lines). (b) Plot of the normalized bubble amplitude with (solid lines) and without (dashed lines) nonlinear terms.

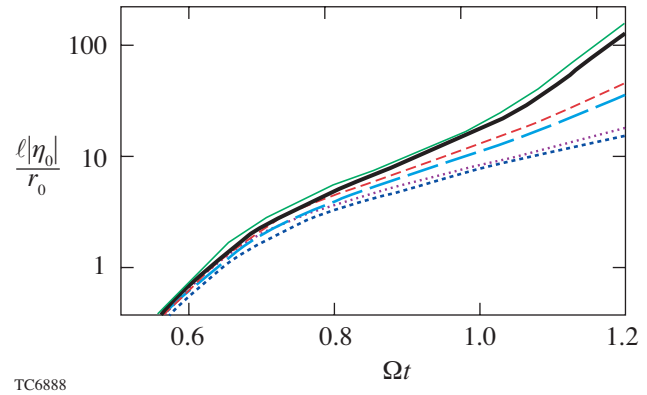

Figure 102.53
Bubble amplitude calculated using the exact numerical solution of Eqs. (30) and (31) (thick lines) and analytical solutions (37) and (48) (thin lines) for ρ = const (solid lines), $\rho \sim 1/r_0$ (dashed lines), and $\rho \sim 1/r_0^2$ (dotted lines).

correspond to $s_\rho = 0, 1,$ and 2, respectively. Note that the bubble growth factors decrease with increasing density. Good agreement between the exact solution and the analytic scaling confirms the accuracy of the asymptotic analysis.

In summary, Layzer's model to study the nonlinear bubble evolution in classical RT instability has been extended to include the temporal density variation and spherical convergence effects. The bubble amplitude in planar geometry with the time-dependent density $\rho(t)$ was shown to asymptote to $\int^t U_L(t')\rho(t')dt'/\rho(t)$, where $U_L = \sqrt{g/C_g k}$ and $C_g = 3$ and $C_g = 1$ for two- and three-dimensional geometries, respectively. The model applied to the spherical geometry predicted the nonlinear bubble amplitude

$$\eta \sim \bar{\eta}(t)\left[m(t)/m_s\right]^{-|\dot{r}_0|/\ell U_L^{sp} - \bar{\eta}/r_0},$$

where r_0 is the outer shell radius,

$$\bar{\eta}(t) = \int^t U_L^{sp}(t')\rho(t')r_0^2(t')dt' \Big/ \rho(t)r_0^2(t),$$

$$U_L^{sp}(t) = \sqrt{-\ddot{r}_0(t)r_0(t)/\ell},$$

$$m(t) = \rho(t)r_0^3(t),$$

$$m_s = m(t_s),$$

t_s is the saturation time, and ℓ is the mode number.

ACKNOWLEDGMENT

This work was supported by the U.S. Department of Energy Office of Inertial Confinement Fusion under Cooperative Agreement No. DE-FC52-92SF19460, the University of Rochester, and the New York State Energy Research and Development Authority. The support of DOE does not constitute an endorsement by DOE of the views expressed in this article.

REFERENCES

1. J. D. Lindl, *Inertial Confinement Fusion: The Quest for Ignition and Energy Gain Using Indirect Drive* (Springer-Verlag, New York, 1998); S. Atzeni and J. Meyer-ter-Vehn, *The Physics of Inertial Fusion: Beam Plasma Interaction, Hydrodynamics, Hot Dense Matter*, International Series of Monographs on Physics (Clarendon Press, Oxford, 2004).

2. B. A. Remington *et al.*, Phys. Plasmas **7**, 1641 (2000).

3. Lord Rayleigh, in *Scientific Papers* (Cambridge University Press, Cambridge, England, 1900), Vol. II, pp. 200–207.

4. D. Layzer, Astrophys. J. **122**, 1 (1955).

5. D. Oron *et al.*, Phys. Plasmas **8**, 2883 (2001); U. Alon *et al.*, Phys. Rev. Lett. **74**, 534 (1995); G. Dimonte, Phys. Plasmas **7**, 2255 (2000); G. Dimonte and M. Schneider *et al*, Phys. Fluids **12**, 304 (2000).

6. G. Dimonte, Phys. Rev. E **69**, 056305 (2004); G. Dimonte *et al.*, Phys. Fluids **16**, 1668 (2004).

7. K. O. Mikaelian, Phys. Rev. Lett. **80**, 508 (1998); K. O. Mikaelian, Phys. Rev. E **67**, 026319 (2003).

8. Q. Zhang, Phys. Rev. Lett. **81**, 3391 (1998).

9. V. N. Goncharov, Phys. Rev. Lett. **88**, 134502 (2002).

10. Y. Yedvab *et al.*, presented at the 6th International Workshop on the Physics of Compressible Turbulent Mixing, Marseille, France, 18–21 June 1997, pp. 528–533.

11. D. Clark and M. Tabak, Bull. Am. Phys. Soc **49**, 281 (2004).

12. N. A. Inogamov and S. I. Abarzhi, Physica D **87**, 339 (1995); S. I. Abarzhi, Phys. Rev. E **59**, 1729 (1999).

13. G. Hazak, Phys. Rev. Lett. **76**, 4167 (1996); A. L. Velikovich and G. Dimonte, Phys. Rev. Lett. **76**, 3112 (1996).

14. G. I. Bell, Los Alamos National Laboratory, Los Alamos, NM, Report LA-1321 (1951).

15. V. N. Goncharov, P. McKenty, S. Skupsky, R. Betti, R. L. McCrory, and C. Cherfils-Clérouin, Phys. Plasmas **7**, 5118 (2000).

16. C. M. Bender and S. A. Orszag, *Advanced Mathematical Methods for Scientists and Engineers* (McGraw-Hill, New York, 1978), p. 484.

17. S. W. Haan, Phys. Rev. A, Gen. Phys. **39**, 5812 (1989).

18. R. Epstein, Phys. Plasmas **11**, 5114 (2004).

19. P. Amendt *et al.*, Phys. Plasmas **10**, 820 (2003).